Engineering 6 (2020) 132–140

Contents lists available at ScienceDirect

Engineering

journal homepage: www.elsevier.com/locate/eng

Research
Rare Earth Permanent Magnets—Review

Structural and Magnetic Properties of Nanocomposite Nd–Fe–B Prepared by Rapid Thermal Processing

Jinbo Yang [a,b,c,*], Jingzhi Han [a,b,c], Haidong Tian [a,b,c], Liang Zha [a,b,c], Xiongzuo Zhang [a,b,c], Chol Song Kim [a,b,c], Dong Liang [a,b,c], Wenyun Yang [a,b,c], Shunquan Liu [a,b,c], Changsheng Wang [a,b,c,*]

[a] State Key Laboratory for Artificial Microstructure and Mesoscopic Physics, School of Physics, Peking University, Beijing 100871, China
[b] Collaborative Innovation Center of Quantum Matter, School of Physics, Peking University, Beijing 100871, China
[c] Beijing Key Laboratory for Magnetoelectric Materials and Devices, Collegue of Engineering, Peking University, Beijing 100871, China

ARTICLE INFO

Article history:
Received 22 August 2018
Revised 11 November 2018
Accepted 11 March 2019
Available online 18 December 2019

Keywords:
Nanocomposites
Electron-beam heating
Landau model and Langevin dynamics simulation
Synergetic crystallization

ABSTRACT

Nanoscale permanent magnetic materials, which possess excellent magnetic and mechanical properties, thermal stability, and corrosion resistance, have become a research hotspot for permanent magnets. In reality, however, the obtained maximum energy product, $(BH)_{max}$, is not satisfactory in comparison with the theory limit, especially for exchange-coupled nanocomposite magnets. The construction of an ideal microstructure still remains a challenge in the synthesis and preparation of nanoscale permanent magnets. This work reported the impact of rapid thermal process (RTP) with electron-beam heating on the microstructures of $Nd_{12.5-x}Fe_{80.8+x}B_{6.2}Nb_{0.2}Ga_{0.3}$ (x = 0, 2.5) nanocomposites. It was found that the crystallization time was greatly reduced, from 15 min under the conventional annealing conditions to 0.1 s under the RTP. For $Nd_2Fe_{14}B$ single-phase materials, the crystallization temperature of the RTP ribbons decreased by about 248 °C compared with that of the ribbons produced by the conventional annealing method. A synergetic crystallization of the $Nd_2Fe_{14}B$ and α-Fe phases was observed under the RTP, which restrained not only the shape, size distribution, and compositions of the hard and the soft phases, but also the interface between them. This modification effect became more obvious as the fraction of Fe increased. Due to the improvement in the uniformity of the $Nd_2Fe_{14}B$ and α-Fe phases, and their grain size distribution, better magnetic properties were achieved using RTP in comparison with the conventional annealing method.

1. Introduction

Permanent magnets are one of the most important materials in modern technology and are widely used in both industrial systems and daily life. For example, permanent magnets are extensively used in electric vehicles and wind turbines in the field of renewable energy, and are used to achieve the miniaturization, lightweight, and energy efficiency required in electronic devices in emerging green-energy-related applications [1,2]. In 1984, Sagawa et al. [3,4] and Croat et al. [5,6] prepared ternary iron-based $Nd_2Fe_{14}B$ magnets with a high maximum energy product, which exhibited excellent performance around room temperature. However, in practical applications, due to the low Curie temperature (~300 °C) of $Nd_2Fe_{14}B$, a large quantity of heavy rare earth elements such as dysprosium (Dy) and terbium (Tb) is required to compensate for the temperature effect on the coercivity, so that doped $Nd_2Fe_{14}B$ can be used at a temperature higher than 100 °C [7–21]. Since heavy rare earth resources are very scarce, great efforts have been made to reduce the doping amount of heavy rare earth elements in Nd–Fe–B permanent magnets [22–24]. Therefore, the innovative design and development of new types of permanent magnets with good performance—especially at high temperatures without (or with a smaller amount of) heavy rare earth elements—has become a top priority.

Nanostructured permanent magnets, and particularly exchange-coupled nanocomposite magnets [25–29], have a very high theoretical maximum energy product and good temperature stability with a reduced ratio of rare earth to transitional elements, and are thus a possible direction in the development of high-performance permanent magnets. In 1989, Coehoorn et al. [25] first prepared $Nd_2Fe_{14}B/Fe_3B$ nanocomposite magnets by rapidly

* Corresponding authors.
E-mail addresses: jbyang@pku.edu.cn (J. Yang), wangcs@pku.edu.cn (C. Wang).

https://doi.org/10.1016/j.eng.2019.12.008

quenching $Nd_4Fe_{78}B_{18}$ alloy, and identified the remanence enhancement effect. Subsequently, Kneller and Hawig [26] theoretically analyzed this material and reported that the microstructure is an important factor affecting the magnetic properties of this two-phase system. Exchange-coupled nanocomposite magnets with an appropriate microstructure combine the advantages of the hard magnetic phase ($R_2Fe_{14}B$, R: rare earth) and the soft magnetic phase (α-Fe, Fe_3B, etc.) to obtain better magnetic performance than single-phase materials. In order to obtain the appropriate microstructure, especially in bulk exchange-coupled materials, in addition to directly quenching the alloy into the exchange-coupled magnet, the alloys may be first quenched into an amorphous state, and then subjected to annealing to prepare the magnets [30,31]. In single-phase $R_2Fe_{14}B$ materials, the microstructure and magnetic properties of samples prepared by annealing in the amorphous state are similar to those resulting from the direct quenching method [32]. However, for amorphous iron (Fe)-rich R–Fe–B materials (R < 11.7 at%), the α-Fe phase is normally nucleated first, and grows quickly during the conventional annealing process [33–35], causing the α-Fe grains to reach a size of 80–100 nm [36–38]. The overgrown α-Fe grains cause degradation of the magnetic properties due to the weak exchange coupling between the hard and soft phases. In Nd–Fe–B-based [38–40] or Pr–Fe–B-based [36,41–43] exchange-coupled magnets, the addition of a small amount of zirconium (Zr) or niobium (Nb) can effectively control grain sizes of 2:14:1 phase and the α-Fe phase in the traditional annealing process, thus improving the magnetic properties [44–47]. An energy product of $(BH)_{max}$ = 178 $kJ{\cdot}m^{-3}$ was reported for Pr–Fe–B-based exchange-coupled isotropic nanocomposite powder [48].

To prepare nanocomposite magnets, an annealing process is normally required in order to crystallize the amorphous precursors. Desirable phases and microstructures need to be obtained since the magnetic properties of the materials are closely related to the phases and their microstructural properties. Therefore, appropriate annealing conditions, including heating and cooling rates, temperature, and time are essential in order to achieve good magnetic properties. The conventional annealing method typically has the characteristics of low heating and cooling rates (generally below 1 $K{\cdot}s^{-1}$). Since slow heating and cooling rates extend the annealing time, grain growth is very common during traditional annealing methods. On the other hand, the rapid thermal process (RTP) permits high heating and cooling rates, which can effectively inhibit the growth of crystal grains; thus, RTP is beneficial for regulating the crystallization, phase compositions, grain size, and morphology [46–69].

Wu et al. [61] studied the effect of a heating rate of up to 5 $K{\cdot}s^{-1}$ on the crystallization of $Nd_{4.5}Fe_{73}B_{18.5}Co_2Cr_2$ amorphous ribbon. The grain size was 30 nm at a lower heating rate, while the grain size was only 15 nm at a higher heating rate, leading to higher remanence, higher coercivity, and a higher maximum energy product. Chromium (Cr)-doped $Nd_2Fe_{14}B/Fe_3B$ nanocomposite magnets have been prepared by means of rapid heat treatment with a heating rate of 5.3 $K{\cdot}s^{-1}$ [68,69]. In these experiments, the heating rate was not particularly fast (1–6 $K{\cdot}s^{-1}$), and the correspondence between the grain size and the rate of temperature increase was not well understood. $(Nd,Tb)_2Fe_{14}B/Fe_3B$ exchange-coupled magnets were prepared by quenching and rapid annealing with a much higher heating rate of 15–25 $K{\cdot}s^{-1}$ [70–72]. Better magnetic properties were achieved using faster heating rates. Chu et al. [67] used iodine–tungsten lamps with a heating rate of about 200 $K{\cdot}s^{-1}$ and a cooling rate of about 150 $K{\cdot}s^{-1}$ to synthesize Nd–Fe–B exchange-coupled magnets, demonstrating that the crystallization process of Nd–Fe–B magnets could be completed in very short time of 1 s. The coercivity of the sample obtained under the conditions of the rapid heat treatment was 10.2 kOe (1 Oe = 79.6 $A{\cdot}m^{-1}$), which was higher than the coercivity of the sample obtained through the conventional annealing method (9.5 kOe). For an iodine–tungsten lamp system, the shortest time interval is about 1 s. A faster heating rate can suppress the growth of the soft magnetic phase, allowing better magnetic properties to be obtained. Jin et al. [72] prepared $Pr_2Fe_{14}B/α$-Fe nanocomposite magnets by using a joule heating treatment on $Pr_7Tb_1Fe_{85}Nb_{0.5}Zr_{0.5}B_6$ amorphous ribbon with a heating rate higher than 350 $K{\cdot}s^{-1}$. They found that the magnetic performance was 30% higher than the values obtained through conventional furnace heating.

As an RTP method, electron-beam heating has very high energy and can generate a very high heating rate (> 1000 $K{\cdot}s^{-1}$). At the same time, precise computer control can be used to set the annealing time to 0.1 s, which is very suitable for studying the annealing effect on amorphous Nd–Fe–B ribbons [73]. Therefore, we chose to prepare single-phase $Nd_2Fe_{14}B$ and two-phase $Nd_2Fe_{14}B/α$-Fe exchange-coupled magnets by means of the electron-beam heating method. Regulation of the grain size, shape, distribution, structure, and composition of the hard and soft magnetic phases was realized in the experiments by means of electron-beam heating with an extremely fast heating rate and a short annealing time. The crystallization process under the conditions of electron-beam heating has been described using the framework of the Landau model and Langevin dynamics simulation, and will be compared with the crystallization process under conventional annealing conditions.

2. Material and methods

Amorphous $Nd_{12.5-x}Fe_{80.8+x}B_{6.2}Nb_{0.2}Ga_{0.3}$ (x = 0, 2.5) ribbons were prepared by quenching melted ingots with a speed of 45 $m{\cdot}s^{-1}$ under an argon (Ar) atmosphere. Two different methods were used for annealing these ribbons: ① In the conventional annealing method, some of the ribbons were annealed with different temperatures and times in an Ar atmosphere using a conventional tube furnace. ② In the RTP method, the as-prepared ribbons were put onto a tungsten plate with water cooling in the vacuum chamber of an electron-beam heating system. The annealing conditions were controlled by adjusting the electron-beam current and the accelerating voltage under a pressure below 5×10^{-3} Pa. The ramping time was 0.1 s, and the annealing time was controlled to within 0.1 s using a computer. Magnetic measurements were performed using an alternating gradient magnetometer (AGM) and a vibrating-sample magnetometer (VSM) at room temperature (RT). A Henkel plot δM was obtained by measuring a series of magnetic hysteresis loops and was calculated as $\delta M = [2M_r(H) + M_d(H)]/M_r(H) - 1$, where $M_r(H)$ is the remanence obtained after the application and subsequent removal of the applied field H on the thermally demagnetized samples. $M_d(H)$ is obtained after magnetic saturation in one direction and the subsequent application and removal of a field H in the reverse direction. The crystal structure and microstructural measurements were obtained using X-ray diffraction (XRD, X'Pert Pro) with Cu-Kα radiation and transmission electron microscopy (TEM, JEM-2010F). The surface morphology and magnetic domains of the sample were observed using an atomic force microscope (AFM) and a magnetic force microscope (MFM).

3. Results and discussion

The XRD patterns of the $Nd_{12.5}Fe_{80.8}B_{6.2}Nb_{0.2}Ga_{0.3}$ ribbons prepared before and after electron-beam heating are shown in Fig. 1. As shown in Fig. 1(a), the $Nd_{12.5}Fe_{80.8}B_{6.2}Nb_{0.2}Ga_{0.3}$ ribbon was amorphous before electron-beam heating, which is verified by the soft magnetic characteristics shown in Fig. 1(c). Broadening diffraction peaks corresponding to the tetragonal $Nd_2Fe_{14}B$ phase

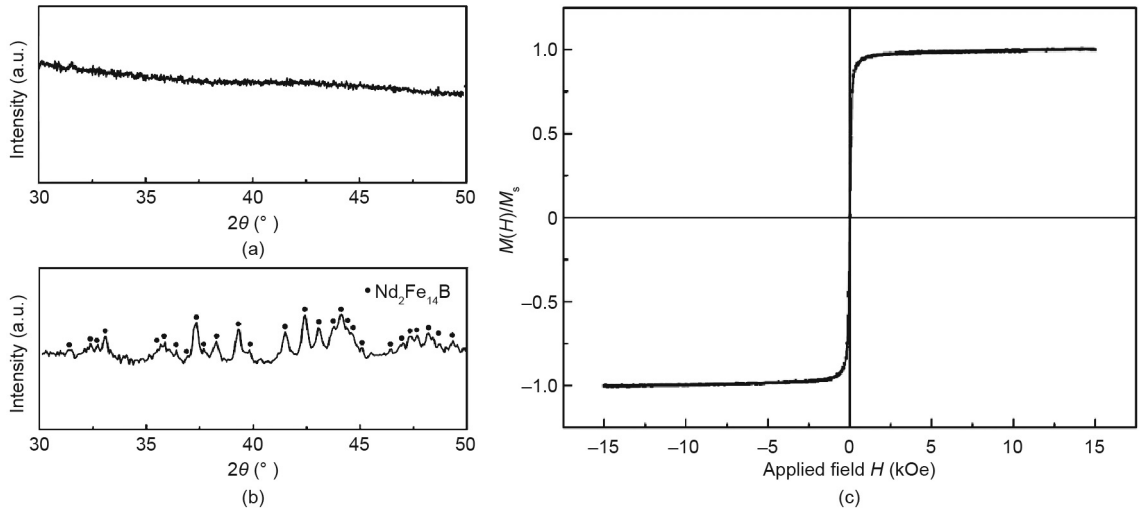

Fig. 1. XRD patterns of the $Nd_{12.5}Fe_{80.8}B_{6.2}Nb_{0.2}Ga_{0.3}$ ribbons prepared (a) before and (b) after electron-beam heating; (c) hysteresis loop of the amorphous $Nd_{12.5}Fe_{80.8}B_{6.2}Nb_{0.2}Ga_{0.3}$ ribbons at RT. $M(H)$: the measured magnetization under applied field H; M_s: the saturation magnetization.

can be seen (Fig. 1(a)), indicating that an amorphous to nanocrystalline state transition was achieved in 0.1 s. This transition was very quick, as diffusion and crystallization processes are normally very slow in solid-state bulk materials. During the RTP with electron-beam heating, localized high-energy electrons collide intensely with the surface and diffuse into the thin ribbon, which transforms their kinetic energy into heat very quickly. The electron beam is focused onto a small diameter (D = 2 mm) on the ribbon surface, and the penetration depth of the electrons in the target can reach several micrometers. Consequently, the heating rate for this volume can reach 10^4 K·s^{-1} (in our case, 512 °C over 0.1 s). Driven by the large thermal gradient and the very high heating rate, the annealing time can be significantly decreased to 0.1 s under the electron-beam heating conditions.

The optimal conventional annealing conditions for the $Nd_{12.5}Fe_{80.8}B_{6.2}Nb_{0.2}Ga_{0.3}$ ribbons were 760 °C for 15 min, and the optimal electron-beam heating conditions were an accelerating voltage of 10 kV, a electron-beam current of 1.8 mA, and a time of 0.1 s. Fig. 2 shows the magnetic properties of $Nd_{12.5}Fe_{80.8}B_{6.2}Nb_{0.2}Ga_{0.3}$ under the optimal electron-beam heating conditions and optimal conventional annealing conditions. It can be seen that the coercivity of the sample increased from 10.6 kOe for conventional annealing to 12.6 kOe for electron-beam heating. The initial magnetization curves and their corresponding first derivate are plotted in Figs. 2(b) and (c) under different annealing conditions. The maximum values of the first derivative were 10.0 and 6.1 kOe for the electron-beam heating sample and conventional annealing sample, respectively, indicating that a stronger pinning effect was caused by the rapid heating rate in the case of electron-beam heating. Localized damage or defect might have occurred due to the microstrain induced in the grains as a result of the extremely fast heating rate. This is consistent with the high coercivity of the sample under the electron-beam heating conditions, in comparison with the sample under the conventional annealing conditions. Fig. 3 shows the magnetic domains and surface morphology of the demagnetized $Nd_{12.5}Fe_{80.8}B_{6.2}Nb_{0.2}Ga_{0.3}$ ribbons after the different annealing processes. The average magnetic domain size of the samples produced by electron-beam heating was significantly smaller than those produced by the conventional annealing method. The actual grain size was about 80 nm for electron-beam heating and

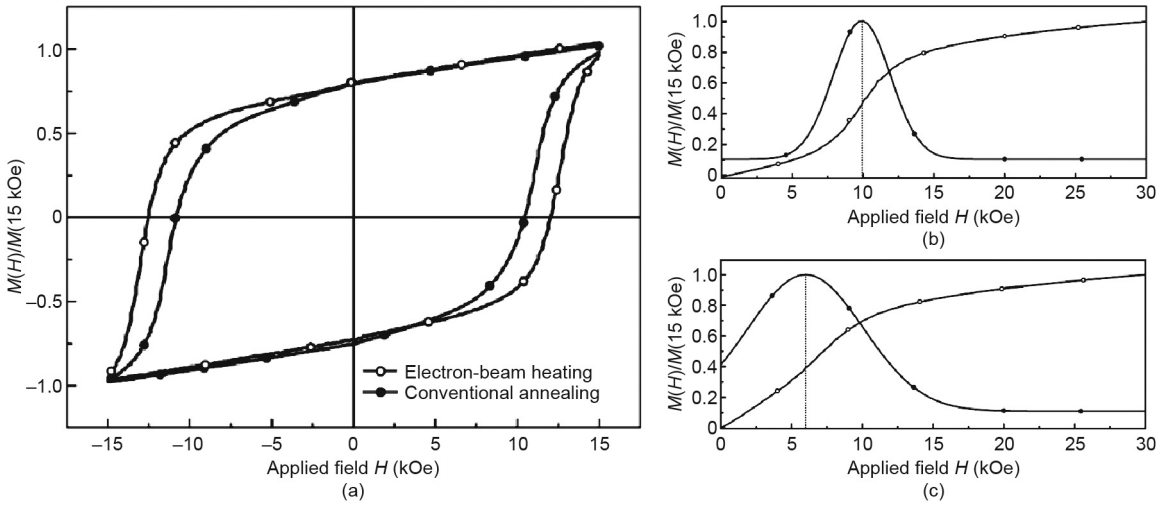

Fig. 2. (a) Hysteresis loops of $Nd_{12.5}Fe_{80.8}B_{6.2}Nb_{0.2}Ga_{0.3}$ under optimal electron-beam heating and optimal conventional annealing conditions. Initial magnetization curve of $Nd_{12.5}Fe_{80.8}B_{6.2}Nb_{0.2}Ga_{0.3}$ under (b) optimal electron-beam heating conditions and (c) optimal conventional annealing conditions. In (b) and (c), the line of hollow dots is the initial magnetization curve, and the line of solid dots is the first derivative of the initial magnetization curve.

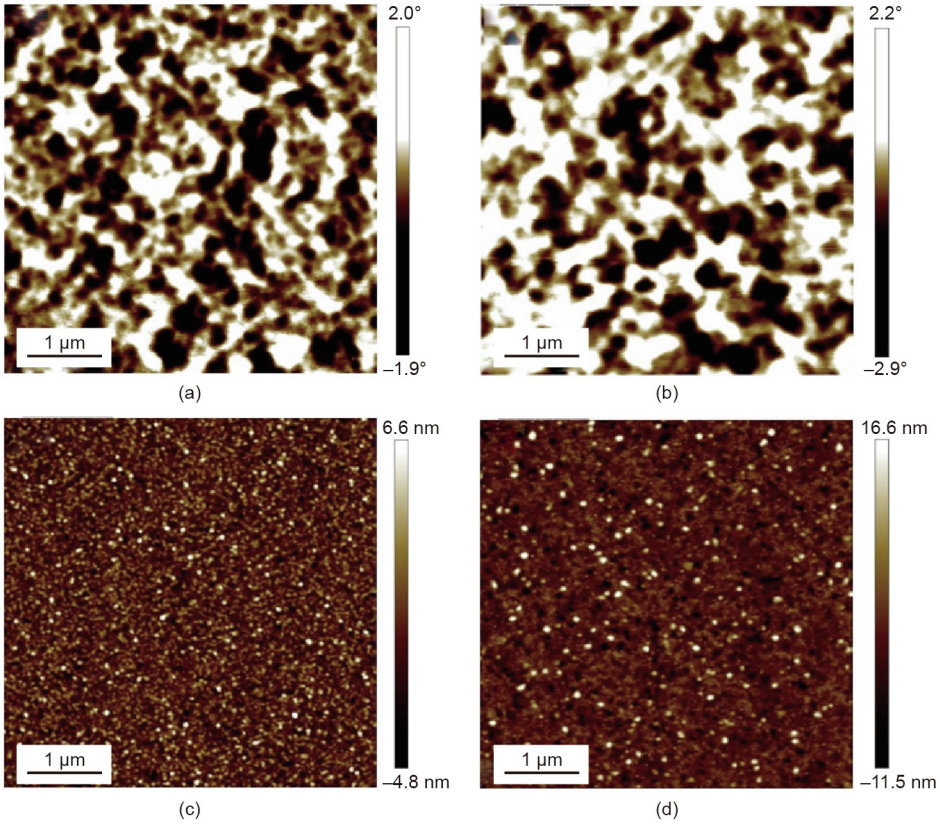

Fig. 3. MFM and AFM images of the $Nd_{12.5}Fe_{80.8}B_{6.2}Nb_{0.2}Ga_{0.3}$ ribbons produced by different annealing methods: Magnetic domain under (a) electron-beam heating conditions and (b) conventional annealing conditions; surface morphology under (c) electron-beam heating conditions and (d) conventional annealing conditions.

about 90 nm for conventional annealing (see later). The samples from both treatments were composed of equiaxed crystals, and the microscopic morphology did not differ significantly. In both cases, the magnetic domain sizes were clearly much larger than the corresponding grain sizes, indicating that typically exchanged domains were formed due to the strong exchange interactions among the grains.

Since the single-domain particle size of the Nd–Fe–B was around 300 nm, the average grain sizes of the annealed ribbons were much smaller than the single-domain size. The intergranular interactions become very important in the determination of the final hard magnetic properties. Therefore, the Henkel plot of the ribbons was obtained to investigate the exchange coupling between the grains. Fig. 4 shows the Henkel plot (δM) of the samples under optimal electron-beam heating conditions and optimal conventional annealing conditions, respectively. The maximums of the δM curves are positive, indicating that intergranular exchange coupling is dominant in these ribbons. The value of the sample produced by electron-beam heating is higher than that of the sample produced by conventional annealing, indicating that the exchange coupling between the sample grains is stronger under electron-beam heating. This result may be due to smaller grains with homogeneous size distribution and stronger pinning effects being generated by defects or microstrain (as shown in Fig. 5) under the electron-beam heating conditions, resulting in stronger exchange coupling between the grains.

Fig. 5 shows typical TEM images of the samples under different annealing conditions. The average grain size of the electron-beam heating sample is about 80 nm (Fig. 5(b)), and the grains all show a regular equiaxed morphology. For the sample from the conventional annealing method, the average grain size is about 90 nm (Fig. 5(a)). It can be seen that there is not much difference in the

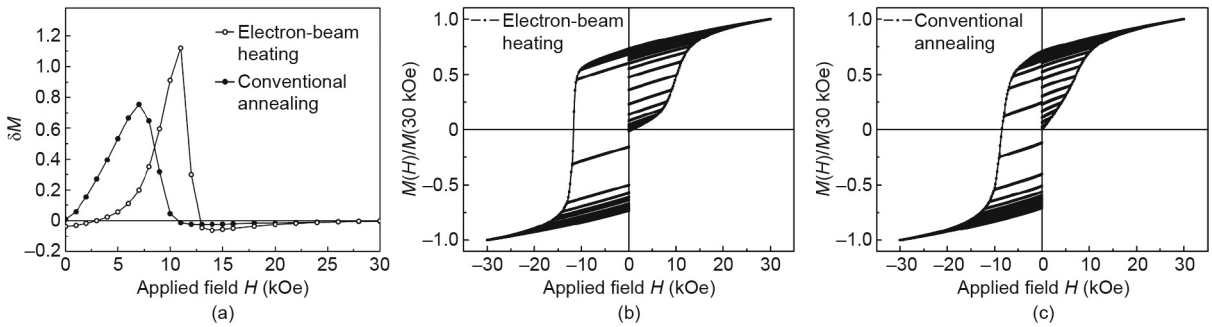

Fig. 4. (a) Henkel plot δM of $Nd_{12.5}Fe_{80.8}B_{6.2}Nb_{0.2}Ga_{0.3}$ ribbons at RT under optimal electron-beam heating and optimal conventional annealing conditions. The original demagnetization loops and recoil loops under (b) optimal electron-beam heating conditions and (c) optimal conventional annealing conditions.

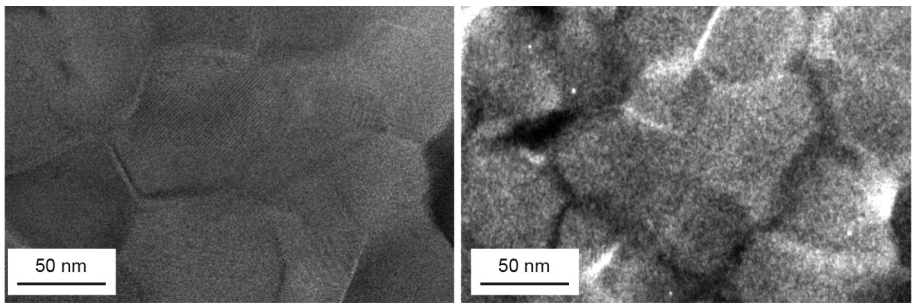

Fig. 5. TEM images of the $Nd_{12.5}Fe_{80.8}B_{6.2}Nb_{0.2}Ga_{0.3}$ ribbons under (a) conventional annealing conditions at 760 °C for 15 min, and (b) electron-beam heating conditions with an accelerating voltage of 10 kV and a current of 1.8 mA for 0.1 s [73].

micro-morphology of the samples produced by the different methods, except that the grain size was reduced so that the coercivity of the sample produced by the electron-beam heating method was improved. Electron-beam heating can provide sufficient energy for the occurrence and maintenance of the crystallization process of $Nd_2Fe_{14}B$ grains through the extremely high beam energy. The annealing time was significantly reduced, from 15 min for the conventional annealing method to 0.1 s for electron-beam heating, which can inhibit the growth of grains and refine the grains. However, we found that the inhibition of grain growth during the crystallization of $Nd_{12.5}Fe_{80.8}B_{6.2}Nb_{0.2}Ga_{0.3}$ was also greatly reduced by decreasing the annealing time, as shown in Fig. 5.

The crystallization process of the $Nd_2Fe_{14}B$ phase can be explained using the theoretical framework of the Landau model and Langevin dynamics simulation [73]. For the annealed $Nd_{12.5}Fe_{80.8}B_{6.2}Nb_{0.2}Ga_{0.3}$ ribbons, the final state contains mainly the $Nd_2Fe_{14}B$ phase, which is a polycrystalline system. During the annealing process, the grains interact with each other because of the mismatch produced by different crystal orientations. The crystallization energy of each grain is slightly different, and the exothermal peak of the $Nd_2Fe_{14}B$ phase will become broad in the differential scanning calorimetry (DSC) curve [74]. This energy difference can be compensated by the low heating rate of conventional annealing. Thus, under conventional annealing, the grains of single-phase $Nd_2Fe_{14}B$ could be crystallized synergistically. The equiaxial grains (Fig. 5(a)) are formed due to the interactions among the grains during the synergetic crystallization process. Synergetic crystallization was observed for single-phase $Nd_2Fe_{14}B$ under both the electron-beam heating and conventional annealing conditions. However, the interactions among the grains became much stronger under the electron-beam heating conditions because of the greater uniformity of the synergetic crystallization of the $Nd_2Fe_{14}B$ grains under the extremely high heating rate, which may help to confine the grain size at 80 nm (see Fig. 5(b)) in additional to the short annealing time. Normally, the effect of interactions on the grain size in a single-phase material is rather small in comparison with the effect of grain growth, so modification of the grain size and morphology is limited. Therefore, we further investigated a system with higher Fe content, $Nd_{10}Fe_{83.3}B_{6.2}Nb_{0.2}Ga_{0.3}$, in which a multi-phase composite can be more easily formed.

For the $Nd_{10}Fe_{83.3}B_{6.2}Nb_{0.2}Ga_{0.3}$ ribbons, the optimal annealing conditions were 730 °C for 15 min for conventional annealing, and an accelerating voltage of 10 kV, a beam current of 2.3 mA, and a time of 0.1 s for electron-beam heating. After electron-beam heating, the coercivity increased by 48%, from 4.56 to 6.73 kOe, and the $M(H)/M$(15 kOe) also increased. Therefore, from the enhancement of the remanence, it can be concluded that the exchange-coupling effect is much stronger in the electron-beam heating sample. The initial magnetization curves and their corresponding first derivate are plotted in Figs. 6(b) and (c) under different annealing conditions. The maximum values of the first derivative were 5.76 and 4.24 kOe for the electron-beam heating sample and conventional annealing sample, respectively, indicating a stronger exchange-coupling effect in the electron-beam heating sample. This result is consistent with the high coercivity of the sample under electron-beam heating in comparison with

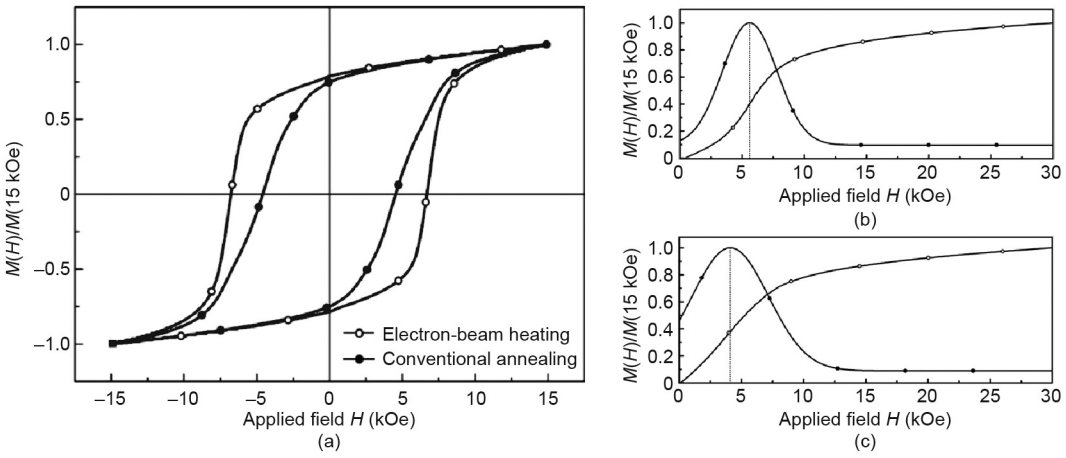

Fig. 6. (a) Hysteresis loops of $Nd_{10}Fe_{83.3}B_{6.2}Nb_{0.2}Ga_{0.3}$ under optimal electron-beam heating and optimal conventional annealing conditions. Initial magnetization curve of $Nd_{10}Fe_{83.3}B_{6.2}Nb_{0.2}Ga_{0.3}$ alloy under (b) optimal electron-beam heating conditions and (c) optimal conventional annealing conditions [73]. In (b) and (c), the line of hollow dots is the initial magnetization curve, and the line of solid dots is the first derivative of the initial magnetization curve.

the sample under conventional annealing. Fig. 7 shows the Henkel plot for the $Nd_{10}Fe_{83.3}B_{6.2}Nb_{0.2}Ga_{0.3}$ sample under different annealing conditions. Similar to the $Nd_{12.5}Fe_{80.8}B_{6.2}Nb_{0.2}Ga_{0.3}$ ribbons, a much stronger intergranular exchange-coupling effect was observed for the electron-beam heating method, as shown in Fig. 7.

Fig. 8 shows the magnetic domains and surface morphology of the $Nd_{10}Fe_{83.3}B_{6.2}Nb_{0.2}Ga_{0.3}$ ribbons under the optimal electron-beam heating and optimal conventional annealing conditions. The size of the magnetic domain under electron-beam heating is larger than that under conventional annealing. A very large domain with a length greater than several micrometers can be observed under the optimal electron-beam heating conditions (Fig. 8(a)). The domain sizes are much larger than the grain size, indicating the characteristic of exchanged magnetic domains in these nanocomposite magnets. Fig. 9 provides TEM images of the $Nd_{10}Fe_{83.3}B_{6.2}Nb_{0.2}Ga_{0.3}$ ribbons produced by electron-beam heating and conventional annealing. As shown in Fig. 9, the microscopic morphology of the samples differs greatly for these two treatment methods. Under electron-beam heating, the α-Fe phase exhibits two forms: elongated grains and equiaxed grains. Under the traditional annealing methods, the morphology of the α-Fe phase is mainly composed of equiaxed grains. It can be concluded that soft magnetic grains with the elongated shape having a critical size of 10 nm, partially surrounding the hard magnetic phase, could induce a sufficiently strong exchange interaction [73]. It is the difference in the final microstructure of the system that causes the coupling between the hard magnetic phase and the soft magnetic phase to be different so that the magnetic properties of the electron-beam heating sample are much better than those of the sample produced by the conventional annealing method.

In comparison with the $Nd_{12.5}Fe_{80.8}B_{6.2}Nb_{0.2}Ga_{0.3}$ compound, the $Nd_{10}Fe_{83.3}B_{6.2}Nb_{0.2}Ga_{0.3}$ compound has much higher Fe

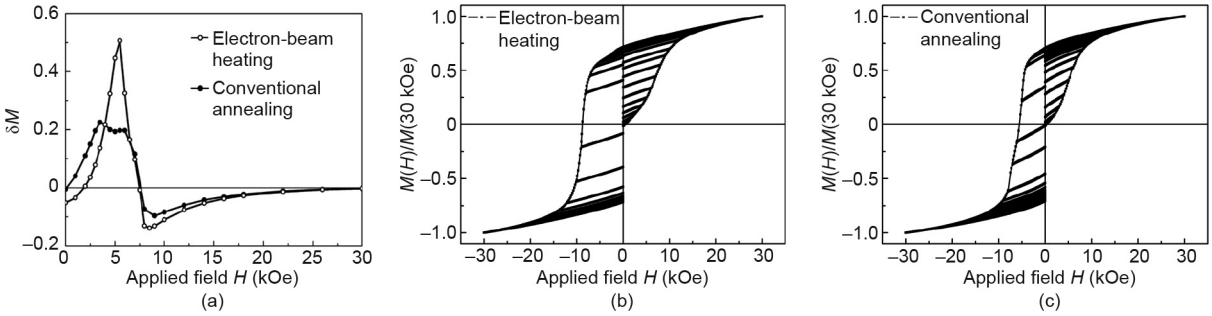

Fig. 7. (a) Henkel plot δM of $Nd_{10}Fe_{83.3}B_{6.2}Nb_{0.2}Ga_{0.3}$ ribbons at RT under optimal electron-beam heating and optimal conventional annealing conditions. The original demagnetization loops and recoil loops under (b) optimal electron-beam heating conditions and (c) optimal conventional annealing conditions.

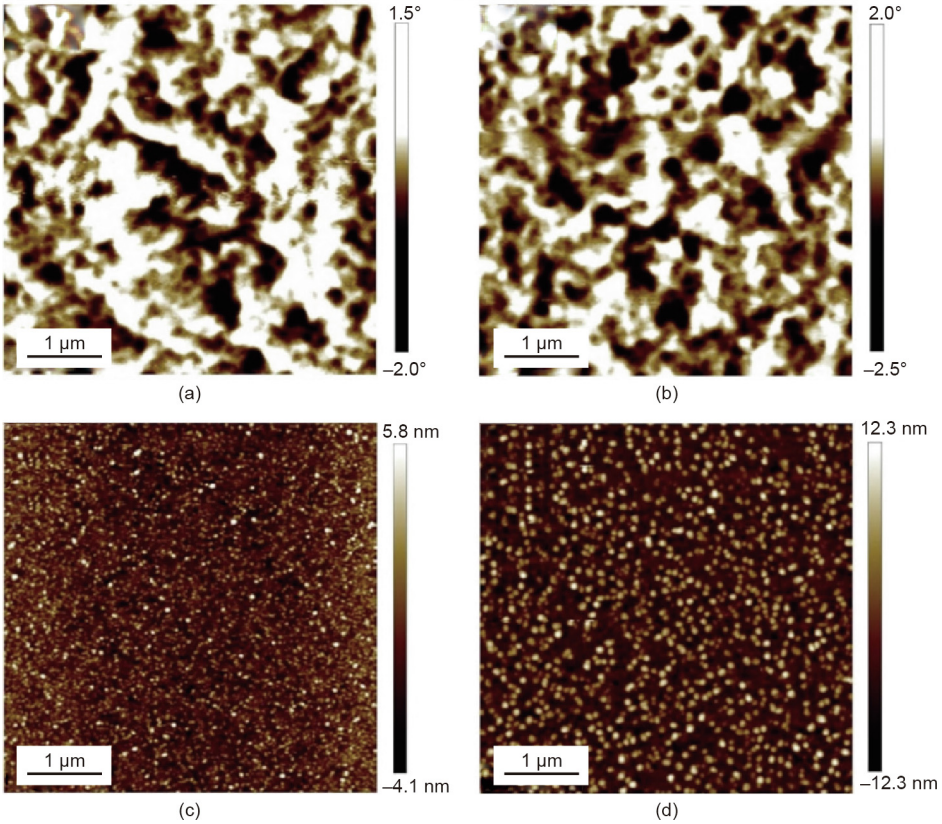

Fig. 8. MFM and AFM images of the $Nd_{10}Fe_{83.3}B_{6.2}Nb_{0.2}Ga_{0.3}$ ribbons under different annealing conditions: Magnetic domain under (a) electron-beam heating conditions and (b) conventional annealing conditions; surface morphology under (c) electron-beam heating conditions and (d) conventional annealing conditions.

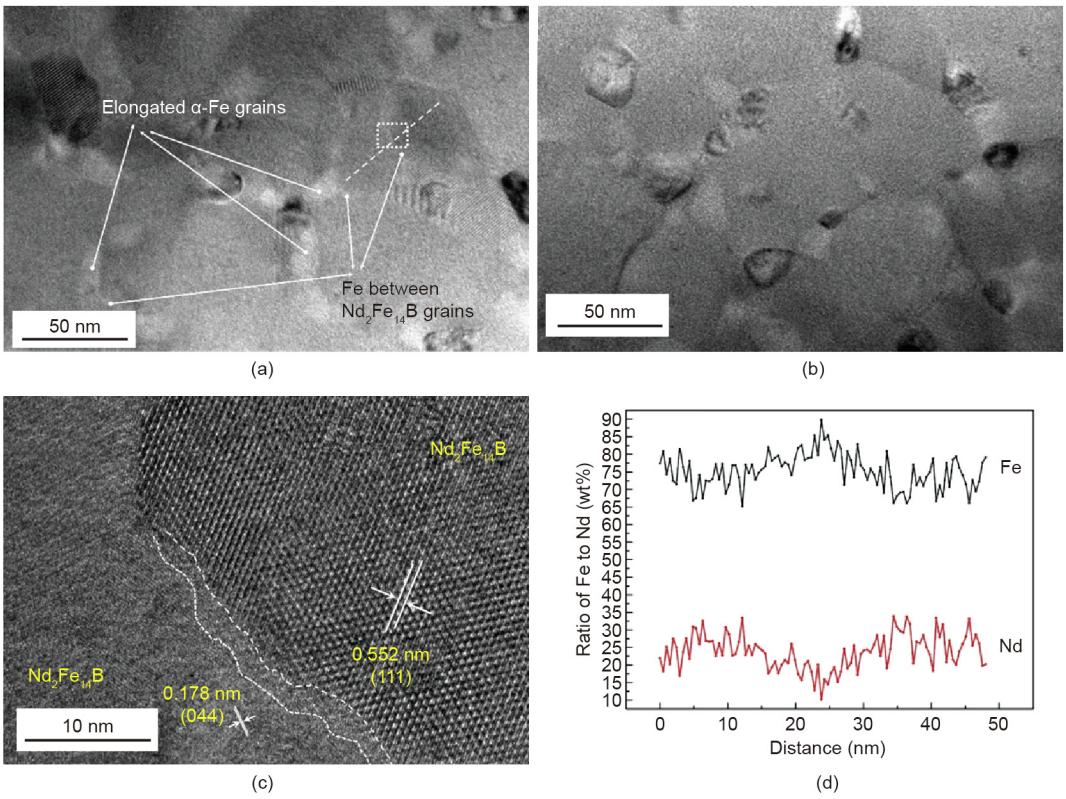

Fig. 9. TEM images of the $Nd_{10}Fe_{83.3}B_{6.2}Nb_{0.2}Ga_{0.3}$ ribbons: (a) Using the electron-beam heating method with an electron-beam current at 2.3 mA and an accelerating voltage at 10 kV for 0.1 s; (b) using the conventional annealing method at 730 °C for 15 min; (c) high resolution TEM (HRTEM) images of the dotted rectangular region in (a); (d) ratio (wt%) of Fe to Nd along the dotted line in (a) [73].

content. Therefore, under the conventional annealing conditions, the grains of the α-Fe phase will crystallize and grow first, leading to weak interactions between the α-Fe and $Nd_2Fe_{14}B$ phases, and weak interactions among the grains. As for the electron-beam heating method, due to the synergetic crystallization of the α-Fe and $Nd_2Fe_{14}B$ phases, the increase of Fe content leads to much more intense interactions between the α-Fe and $Nd_2Fe_{14}B$ phases. This interaction keeps the grains in a regular shape (i.e., equiaxial-like). In the meantime, there are some elongated α-Fe and $Nd_2Fe_{14}B$ nano-grains, which may facilitate strong exchange coupling between the hard and soft phases in the compounds, as shown in Fig. 9(a); therefore, better coercivity and squareness in the hysteresis loop can be achieved due to effective exchange coupling between the hard and soft phases.

4. Conclusions

The magnetic properties and crystallization behavior of the $Nd_2Fe_{14}B$ single-phase and $Nd_2Fe_{14}B$/α-Fe two-phase nanocomposite magnets prepared using electron-beam heating and conventional annealing methods were studied systematically. It was found that the RTP with electron-beam heating can greatly reduce the crystallization time of the amorphous ribbons from about 15 min under the conventional annealing conditions to 0.1 s, due to the extremely high heating rate. For the $Nd_2Fe_{14}B$ single-phase material, the crystallization temperature of the amorphous ribbon can be greatly reduced from 760 °C under the conventional annealing conditions to 512 °C under the electron-beam heating conditions. A strong synergistic crystallization effect of the $Nd_2Fe_{14}B$ and α-Fe phases in the $Nd_2Fe_{14}B$/α-Fe two-phase magnets was observed under electron-beam heating conditions. The amorphous crystallization process can be controlled by the extremely fast heating rate and extremely short annealing time during electron-beam heating, so as to further regulate the grain size, grain shape, and distribution of hard and soft magnetic phases, as well as the structure and composition on the sample and on the interface. The higher the Fe content is, the more obvious this regulation effect is. It was found that the interactions between the $Nd_2Fe_{14}B$ grains, the $Nd_2Fe_{14}B$, and the α-Fe grains during the amorphous crystallization process allow the grains to maintain a regular shape and result in uniform distribution of the crystal grain size. At the same time, the interactions between the $Nd_2Fe_{14}B$ phase and the α-Fe phase grains change the grain shape of the soft magnetic phase and the hard magnetic phase, and cause the Fe to enter between the $Nd_2Fe_{14}B$ phase grains to induce strong exchange coupling. The uniformity of the phase distribution and the smaller grain size can improve the exchange coupling between the hard and soft phases, thereby resulting in better magnetic properties. We propose that the performance of $Nd_2Fe_{14}B$/α-Fe nanocomposite magnets will be further improved if a soft magnetic phase with a width in the critical dimension range can be formed to continuously surround the hard magnetic phase.

Acknowledgements

This work is supported by the National Key Research and Development Program of China (2016YFB0700901 and 2017YFA0206303) and the National Natural Science Foundation of China (51731001, 11805006, and 11675006). This work makes use of the resources of the Beijing National Center for Electron Microscopy at Tsinghua University.

Compliance with ethics guidelines

Jinbo Yang, Jingzhi Han, Haidong Tian, Liang Zha, Xiongzuo Zhang, Chol Song Kim, Dong Liang, Wenyun Yang, Shunquan Liu, and Changsheng Wang declare that they have no conflicts of interest or financial conflicts to disclose.

References

[1] Gutfleisch O, Willard MA, Brück E, Chen CH, Sankar SG, Liu JP. Magnetic materials and devices for the 21st century: stronger, lighter, and more energy efficient. Adv Mater 2011;23(7):821–42.
[2] Buschow KHJ. New developments in hard magnetic materials. Rep Prog Phys 1991;54(9):1123–213.
[3] Sagawa M, Fujimura S, Togawa N, Yamamoto H, Matsuura Y. New material for permanent magnets on a base of Nd and Fe. J Appl Phys 1984;55(6):2083–7.
[4] Sagawa M, Fujimura S, Yamamoto H, Matsuura Y, Hiraga K. Permanent magnet materials based on the rare earth–iron–boron tetragonal compounds. IEEE Trans Magn 1984;20(5):1584–9.
[5] Croat JJ, Herbst JF, Lee RW, Pinkerton FE. Pr–Fe and Nd–Fe-based materials: a new class of high-performance permanent magnets. J Appl Phys 1984;55(6):2078–82.
[6] Croat JJ, Herbst JF, Lee RW, Pinkerton FE. High-energy product Nd–Fe–B permanent magnets. Appl Phys Lett 1984;44(1):148–9.
[7] Herbst JF. $R_2Fe_{14}B$ materials: intrinsic properties and technological aspects. Rev Mod Phys 1991;63(4):819–98.
[8] Kim AS, Camp FE. High performance NdFeB magnets. J Appl Phys 1996;79(8):5035–9.
[9] Marinescu M, Chiriac H, Grigoras M. Magnetic properties of bulk nanocomposite permanent magnets based on NdDyFeB alloys with additions. J Magn Magn Mater 2005;290–291:1267–9.
[10] Gong W, Li Q, Yin L. Temperature feature of NdDyFeB magnets with ultrahigh coercivity. J Appl Phys 1991;69(8):5512–4.
[11] Harland CL, Davies HA. Magnetic properties of melt-spun Nd-rich NdFeB alloys with Dy and Ga substitutions. J Alloys Compd 1998;281(1):37–40.
[12] Pan M, Zhang P, Li X, Ge H, Wu Q, Jiao Z, et al. Effect of terbium addition on the coercivity of the sintered NdFeB magnets. J Rare Earths 2010;28(Suppl 1):399–402.
[13] Kosobudskii ID, Sevost'yanov VP, Kuznetsov MY. Magnetic properties of R-Nd–Fe–B (R = Tb, Dy) and Nd–Fe–Co–B alloys in the range −80 to 250 °C. Inorg Mater 2000;36(6):584–6.
[14] Kim AS. High coercivity Nd–Fe–B magnets with lower dysprosium content. J Appl Phys 1988;63(8):3519–21.
[15] Li S, Gu B, Yang S, Bi H, Dai Y, Tian Z, et al. Thermal behaviour and magnetic properties of B-rich NdFeB nanocomposite hard magnetic alloys with partial substitution of Dy for Nd. J Phys D Appl Phys 2002;35(8):732–7.
[16] Liu Z, Davies HA. Elevated temperature study of nanocrystalline (Nd/Pr)–Fe–B hard magnetic alloys with Co and Dy additions. J Magn Magn Mater 2005;290–1:1230–3.
[17] Gong WJ, Wang X, Liu W, Guo S, Wang ZH, Cui WB, et al. Enhancing the perpendicular anisotropy of NdDyFeB films by Dy diffusion process. J Appl Phys 2012;111(7):07A729.
[18] Kim AS, Camp FE. Effect of minor grain boundary additives on the magnetic properties of NdFeB magnets. IEEE Trans Magn 1995;31(6):3620–2.
[19] Rodewald W, Wall B, Katter M, Uestuener K. Top Nd–Fe–B magnets with greater than 56 MGOe energy density and 9.8 kOe coercivity. IEEE Trans Magn 2002;38(5):2955–7.
[20] Sugimoto S. Current status and recent topics of rare-earth permanent magnets. J Phys D Appl Phys 2011;44(6):064001.
[21] Liu ZW, Davies HA. The practical limits for enhancing magnetic property combinations for bulk nanocrystalline NdFeB alloys through Pr, Co and Dy substitutions. J Magn Magn Mater 2007;313(2):337–41.
[22] Sepehri-Amin H, Ohkubo T, Hono K. Grain boundary structure and chemistry of Dy-diffusion processed Nd–Fe–B sintered magnets. J Appl Phys 2010;107(9):09A745.
[23] Li D, Suzuki S, Kawasaki T, Machida K. Grain interface modification and magnetic properties of Nd–Fe–B sintered magnets. Jpn J Appl Phys 2008;47(10):7876–8.
[24] Nakamura H, Hirota K, Ohashi T, Minowa T. Coercivity distributions in Nd–Fe–B sintered magnets produced by the grain boundary diffusion process. J Phys D Appl Phys 2011;44(6):064003.
[25] Coehoorn R, de Mooij DB, de Waard C. Meltspun permanent magnet materials containing Fe_3B as the main phase. J Magn Magn Mater 1989;80(1):101–4.
[26] Kneller EF, Hawig R. The exchange-spring magnet: a new material principle for permanent magnets. IEEE Trans Magn 1991;27(4):3588–660.
[27] Bader SD. Colloquium: opportunities in nanomagnetism. Rev Mod Phys 2006;78(1):1–15.
[28] Yue M, Zhang X, Liu JP. Fabrication of bulk nanostructured permanent magnets with high energy density: challenges and approaches. Nanoscale 2017;9(11):3674–97.
[29] Zhang X, Zhang J, Wang W. A novel route for the preparation of nanocomposite magnets. Adv Mater 2000;12(19):1441–4.
[30] Tu G, Altounian Z, Ryan DH, Ström-Olsen JO. Crystallization and texturing in rapidly quenched $Nd_2Fe_{14}B_1$ and $Nd_{15}Fe_{77}B_8$. J Appl Phys 1988;63(8):3330–2.
[31] Jha A, Davies HA, Buckley RA. Glass forming ability and kinetics of crystallisation of rapidly quenched Nd–Fe–B alloys. J Magn Magn Mater 1989;80(1):109–14.
[32] Harland CL, Davies HA. Effect of Co and Zr on magnetic properties of nanophase PrFeB alloys. J Appl Phys 2000;87(9):6116–8.
[33] Wang Z, Zhou S, Zhang M, Qiao Y, Wang R. Effects of as-quenched structures on the phase transformations and magnetic properties of melt-spun $Pr_7Fe_{88}B_5$ ribbons. J Appl Phys 1999;86(12):7010–6.
[34] Wang Z, Zhou S, Zhang M, Qiao Y, Gao X, Zhao Q, et al. Microstructure evolution and magnetic properties of overquenched $Pr_8Fe_{86}B_6$ ribbons during annealing. J Appl Phys 1999;85(8):4880–2.
[35] Imai T, Kojima S, Jiang D. High strain rate superplasticity of SiC_p/1100 and SiC_p/1N90 P/M pure aluminum composites. Mater Sci Eng A 1997;225(1–2):184–7.
[36] Chang WC, Hsing DM. Magnetic properties and transmission electron microscopy microstructures of exchange coupled $Nd_{12-x}Fe_{82+x}B_6$ melt spun ribbons. J Appl Phys 1996;79(8):4843–5.
[37] Chen Z, Zhang Y, Ding Y, Hadjipanayis GC, Chen Q, Ma B. Magnetic properties and microstructure of nanocomposite $R_2(Fe,Co,Nb)_{14}B$/(Fe,Co) (R = Nd, Pr) magnets. J Appl Phys 1999;85(8):5908–10.
[38] Yajima K, Nakamura H, Kohmoto O, Yoneyama T. Microstructure of rapidly quenched Nd–Fe–Zr–B magnets. J Appl Phys 1988;64(10):5528–30.
[39] Kohmoto O, Yoneyama T, Yajima K. Magnetic properties of rapidly quenched $Nd_{10}Fe_{85-x}T_xB_5$ (T = Zr, Nb) alloys. Jpn J Appl Phys 1987;26(Pt 1):1804–5.
[40] Chiriac H, Marinescu M, Buschow KHJ, de Boer FR, Bruck E. Nanocrystalline $Nd_8Fe_{77}Co_5CuNb_3B_6$ melt-spun ribbons. J Magn Magn Mater 1999;203(1–3):153–5.
[41] Wu YQ, Ping DH, Hono K, Hamano M, Inoue A. Microstructural characterization of an α-Fe/$Nd_2Fe_{14}B$ nanocomposite magnet with a remaining amorphous phase. J Appl Phys 2000;87(12):8658–65.
[42] Betancourt I, Davies HA. Influence of Zr and Nb dopant additions on the microstructure and magnetic properties of nanocomposite $RE_2(Fe,Co)_{14}B$/α(Fe,Co) (RE = Nd–Pr) alloys. J Magn Magn Mater 2003;261(3):328–36.
[43] Wang C, Yan M, Zhang WY. Effects of Nb and Zr additions on crystallization behavior, microstructure and magnetic properties of melt-spun $(Nd,Pr)_2Fe_{14}B$/α-Fe alloys. J Magn Magn Mater 2006;306(2):195–8.
[44] Yoshizawa Y, Oguma S, Yamauchi K. New Fe-based soft magnetic alloys composed of ultrafine grain structure. J Appl Phys 1988;64(10):6044–6.
[45] McHenry ME, Willard MA, Laughlin DE. Amorphous and nanocrystalline materials for applications as soft magnets. Prog Mater Sci 1999;44(4):291–433.
[46] McGuiness PJ, Short C, Wilson AF, Harris IR. The production and characterization of bonded, hot-pressed and die-upset HDDR magnets. J Alloys Compd 1992;184(2):243–55.
[47] Bollero A, Gebel B, Gutfleisch O, Müller KH, Schultz L, McGuiness PJ, et al. NdDyFeBZr high-coercivity powders prepared by intensive milling and the HDDR process. J Alloys Compd 2001;315(1–2):243–50.
[48] Bollero A, Gutfleisch O, Müller KH, Schultz L, Drazic G. High-performance nanocrystalline PrFeB-based magnets produced by intensive milling. J Appl Phys 2002;91(10):8159.
[49] Zhang XY, Guan Y, Zhang JW, Sprengel W, Reichle KJ, Blaurock K, et al. Evolution of interface structure of α-Fe/$Nd_2Fe_{14}B$ nanocomposites prepared by crystallization from the amorphous alloy. Phys Rev B Condens Matter Mater Phys 2002;66(21):212103.
[50] Zhang XY, Guan Y, Zhang JW. Study of interface structure of α-Fe/$Nd_2Fe_{14}B$ nanocomposite magnets. Appl Phys Lett 2002;80(11):1966–8.
[51] Guo D, Li W, Li X, Chen Y, Sato K, Zhang X. Improving the interfacial structure of nanocomposite magnets on an atomic scale. J Phys D Appl Phys 2010;43(32):325003.
[52] Li W, Li X, Li L, Zhang J, Zhang X. Enhancement of the maximum energy product of α-Fe/$Nd_2Fe_{14}B$ nanocomposite magnets by interfacial modification. J Appl Phys 2006;99(12):126103.
[53] Li W, Li L, Li X, Sun H, Zhang X. Enhanced coercivity in α-(Fe,Co)/$(Nd,Pr)_2Fe_{14}B$ nanocomposite magnets via interfacial modification. J Phys D Appl Phys 2008;41(15):155003.
[54] Zhang Y, Li W, Li H, Zhang X. Coercivity mechanism of α-Fe/$Nd_2Fe_{14}B$ nocomposite magnets with an intergranular amorphous phase. J Phys D Appl Phys 2014;47(1):015002.
[55] Li H, Lou L, Hou F, Guo D, Li W, Li X, et al. Simultaneously increasing the magnetization and coercivity of bulk nanocomposite magnets via severe plastic deformation. Appl Phys Lett 2013;103(14):142406.
[56] Rong CB, Wang D, Nguyen VV, Daniil M, Willard MA, Zhang Y, et al. Effect of selective Co addition on magnetic properties of $Nd_2(FeCo)_{14}B$/α–Fe nanocomposite magnets. J Phys D Appl Phys 2013;46(4):045001.
[57] Yue M, Niu PL, Li YL, Zhang DT, Liu WQ, Zhang JX, et al. Structure and magnetic properties of bulk isotropic and anisotropic $Nd_2Fe_{14}B$/α-Fe nanocomposite permanent magnets with different α-Fe contents. J Appl Phys 2008;103(7):07E101.
[58] Roozeboom F, Dirne FWA. Rapid thermal annealing of amorphous and nanocrystalline soft-magnetic alloys in a static magnetic field. J Appl Phys 1995;77(10):5293–7.
[59] Yu M, Liu Y, Liou SH, Sellmyer DJ. Nanostructured NdFeB films processed by rapid thermal annealing. J Appl Phys 1998;83(11):6611–3.
[60] Jin ZQ, Liu JP. Rapid thermal processing of magnetic materials. J Phys D Appl Phys 2006;39(14):R227–44.
[61] Wu YQ, Ping DH, Murty BS, Kanekiyo H, Hirosawa S, Hono K. Influence of heating rate on the microstructure and magnetic properties of $Fe_3B/Nd_2Fe_{14}B$ nanocomposite magnets. Scr Mater 2001;45(3):355–62.

[62] Murillo N, González J, González JM, de Julián C, Cebollada F. Magnetic hardening of melt-spun 2:14:1-based materials by high heating rate and short time crystallization treatments. J Mater Res 1995;10(2):292–6.
[63] Fang JS, Chin TS, Chen SK. Nanocrystalline $Nd_6Fe_{88-x}M_xB_6$ (M = Ti or V) magnets by rapid thermal annealing. IEEE Trans Magn 1996;32(5):4401–3.
[64] Gao Y, Zhang S, Liu B. Crystallization behavior of melt-spun $Nd_7Fe_{86}Nb_1B_6$ ribbons under different heating rates. J Magn Magn Mater 2000;208(3):158–62.
[65] Kojima A, Makino A, Inoue A. Rapid-annealing effect on the microstructure and magnetic properties of the Fe-rich nanocomposite magnets. J Appl Phys 2000;87(9):6576–8.
[66] Jiang H, O'Shea MJ. The influence of anneal time on exchange-coupling in $Nd_2Fe_{14}B/\alpha$-Fe films. IEEE Trans Magn 2001;37:2579–81.
[67] Chu KT, Jin ZQ, Chakka VM, Liu JP. Rapid magnetic hardening by rapid thermal annealing in NdFeB-based nanocomposites. J Phys D Appl Phys 2005;38(22):4009–14.
[68] Suzuki K, Cadogan JM, Uehara M, Hirosawa S, Kanekiyo H. Effect of Cr content on decomposition behaviour of amorphous $Nd_5Fe_{74}Cr_3B_{18}$. Scr Mater 2000;42(5):487–92.
[69] Suzuki K, Cadogan JM, Uehara M, Hirosawa S, Kanekiyo H. Formation and decomposition of $Fe_3B/Nd_2Fe_{14}B$ nanocomposite structure in Fe–Nd–B–Cr melt-spun ribbons under isothermal annealing. J Appl Phys 1999;85(8):5914–6.
[70] Bernardi J, Soto GF, Fidler J, David S, Givord D. Influence of microstructure on magnetic properties of nanocomposite $RE_{5.5}(Fe,Cr,M)_{76.5}B_{18}$ (RE = Nd, Tb; Cr $\geq$ 3 at%; M = Co, Si) magnetic materials. J Appl Phys 1999;85(8):5905–7.
[71] Bernardi J, Schrefl T, Fidler J, Rijks T, de Kort K, Archambault V, et al. Preparation, magnetic properties and microstructure of lean rare-earth permanent magnetic materials. J Magn Magn Mater 2000;219(2):186–98.
[72] Jin ZQ, Cui BZ, Liu JP, Ding Y, Wang ZL, Thadhani NN. Controlling the crystallization and magnetic properties of melt-spun $Pr_2Fe_{14}B/\alpha$-Fe nanocomposites by Joule heating. Appl Phys Lett 2004;84(22):4382–4.
[73] Tian H, Zhang Y, Han J, Xu Z, Zhang X, Liu S, et al. Synergetic crystallization in a $Nd_2Fe_{14}B/\alpha$–Fe nanocomposite under electron beam exposure conditions. Nanoscale 2016;8(42):18221–7.
[74] Dang EKF, Gooding RJ. Theory of the effects of rapid thermal annealing on thin-film crystallization. Phys Rev Lett 1995;74(19):3848–51.